#### RESEARCH



# Surface-modified gold-coated superparamagnetic iron oxide nanoparticles promoting light-controlled drug release

Tian-Hao Yan<sup>1</sup> · Muzhaozi Yuan<sup>2</sup> · Nguyen Nguyen<sup>2</sup> · Jingfan Chen<sup>2</sup> · Xuhui Feng<sup>2</sup> · Tianzhu Fan<sup>2</sup> · Mackenzie Caitlin Harnett<sup>2</sup> · Zhifeng Xiao<sup>1</sup> · Ying Li<sup>2</sup> · Jean-Philippe Pellois<sup>1,3</sup> · Hong-Cai Zhou<sup>1,4</sup> · Ya Wang<sup>2,5,6</sup>

Received: 4 July 2023 / Revised: 24 September 2023 / Accepted: 3 December 2023 / Published online: 11 December 2023 © The Author(s), under exclusive licence to Springer Nature Switzerland AG 2023

#### **Abstract**

The main translational barrier of neuroprotective drugs such as retinoic acid (RA) is the lack of targeted delivery to the specified brain region and the short half-life. Superparamagnetic iron-oxide (SPIO) coated with solid gold (SPIO@Au) and hollow gold (SPIO@HG) nanoparticles (NPs) have shown promise as brain-specific nanocarriers for sustainable and controlled delivery of neuroprotective drugs. However, their effectiveness has been restricted by their limited loading capacity. Surface functionalization with porous coordinate cages (PCCs) as a premium drug encapsulating component through SH-PEG-Py ligands has the potential to address this issue. Still, the traditional direct exchange (DE) method often results in insufficient functionalized ligands. This paper presents the anion exchange resin (AER)-based surface modification approach that can improve the number of functionalized ligands, regulate NP surface charges, and improve the colloidal stability by facilitating the ligand exchange reactions. This, in turn, has largely enhanced the drug encapsulation capacities of SPIO@Au NPs functionalized with PCCs. The hydrodynamic diameter and ζ-potential have validated the effectiveness of AER-based functionalization of PCCs on both SPIO@Au and SPIO@HG NPs. The colloidal stability of SPIO@Au-PCC NPs exhibits a more positive surface charge (38 mV) than the DE method (-17 mV). The loading capacity of RA with SPIO@Au-PCC has increased by 2.5 times compared with the traditional DE method (32.29 vs. 13.51 µg/mg). The 24-h release of RA has increased to 88% from 55% through a periodic 10-min stimulation using a 100-mW LASER pointer (525 nm). This enables potential light-modulated drug release on demand. Cell viability experiments confirm excellent biocompatibility with>92.5% cell viability of 40 µg/ml SPIO@Au and SPIO@HG NPs in PC-12 neuron-like cells for up to 5 days of incubation. The strong colloidal stability, high drug loading capacity, and controlled drug release profile suggest the potential of AER-assisted surface modification of magneto-plasmonic nanocarriers for controlled drug delivery of neuroprotective drugs.

 $\textbf{Keywords} \ \ \text{Magneto-plasmonic nanocarriers} \cdot \text{Anion exchange resin-based surface functionalization} \cdot \text{Controlled drug delivery} \cdot \text{Light-controlled release}$ 

# 1 Introduction

Neurodegenerative diseases (NDs), particularly Parkinson's and Alzheimer's, are predicted to affect nearly 7.4 million people in the USA by 2030 [1]. Various therapeutic agents

Tian-Hao Yan and Muzhaozi Yuan are the co-first authors.

- Muzhaozi Yuan muzhaozi.yuan@tamu.edu
- Department of Chemistry, Texas A&M University, College Station, TX 77843, USA
- J. Mike Walker '66 Department of Mechanical Engineering, Texas A&M University, College Station, TX 77843, USA

are developed, but their efficacy has been largely limited due to poor brain accumulation [2]. An example is retinoic acid (RA), an essential molecule in the maintenance of gene expression and acts as a promoter of neuronal cell survival, growth [3], and differentiation [4]. Because of these intrinsic properties, RA has been identified as a potential therapeutic

- Department of Biochemistry and Biophysics, Texas A&M University, College Station, TX 77843, USA
- Department of Materials Science and Engineering, Texas A&M University, College Station, TX 77843, USA
- Department of Electrical and Computer Engineering, Texas A&M University, College Station, TX 77843, USA
- Department of Biomedical Engineering, Texas A&M University, College Station, TX 77843, USA



agent in treating NDs. However, its therapeutic efficacy has been limited by low brain accumulation due to its off-targeting [5], low blood–brain barrier (BBB) crossing efficiency [6], poor aqueous solubility, and short half-life [7]. Thus, there is a need to develop a strategy for brain-specific delivery and controlled release of therapeutic agents using smart nanocarriers, such as magneto-plasmonic nanoparticles (MPNPs).

MPNPs can promote BBB crossing efficiency [8], extend the blood circulation time [6], and control the release of drugs through external stimulation like light [9, 10], magnetic field (MF) [11, 12], and focused ultrasound [13, 14]. Light has attracted significant interest in this exogenous stimulus as it is non-invasive and spatiotemporally controllable [15]. One of the promising light-induced drug release mechanisms is through the generation of the plasmonic heat, which utilizes the localized surface plasmonic resonance (SPR) of MPNPs such as silver (Ag) and gold (Au) nanoparticles (NPs) [16, 17]. We have recently proved that superparamagnetic iron oxide (SPIO) NPs coated with solid gold (SPIO@Au) have improved neuronal differentiation, maturation, and growth in PC-12 cells [18, 19]. They also have exhibited a high biostability [20, 21], strong biocompatibility [22, 23], inherent magnetic properties [19], and modifiable surface architectures [24]. In addition, SPIO NPs coated with the hollow gold (SPIO@ HG) [25] can trap multiple SPIO cores and shift the SPR peak to the near-infrared (NIR) region, which can strengthen magnetic momentum and deepen penetration capability [26]. Our recent results in adult mice have demonstrated the brain-targeting ability of intraperitoneal and intravenous injected SPIO@Au [27] and SPIO@HG NPs [28] guided by a MF. We demonstrated that the MF can promote brain accumulation of these MPNPs for up to 1.54 times at 2 h after injection. Our physiologically based pharmacokinetic model can predict such results theoretically and numerically. These features make SPIO@Au and SPIO@HG NPs attractive candidates for brain-specific drug delivery.

To further improve their loading capacity, we functionalized SPIO@Au NPs with porous coordination cages (PCCs) [29]. PCCs have chemical and electrical properties that can be tuned by modifying coordination sites and surface architectures [30] [31]. This benefit allows PCCs with net-negative or net-positive charges and hydrophobic inner cavities to encapsulate hydrophobic molecules such as RA. It also allows controlled and sustained release of RA using low-power light emitting diodes (LEDs) [29]. The synthesized SPIO@Au-Py-PCC NPs still need an improvement on their stability and loading capacity due to insufficient functionalized PCCs onto NPs.

In this regard, we present a single-step method for the ligand exchange at the surface of Au and HG coating using an anionic exchange resin (AER). AER has been reported to

facilitate a ligand exchange reaction of anionic or neutral Au NPs with cationic ligands [32]. In their work, a Cl<sup>-</sup> type AER releases Cl<sup>-</sup> in exchange for citrate from an anionic Au NP, allowing a cationic thiol to take its place on the NP's surface. This is a promising solution for improving the stability of NPs in general. This simplified procedure for NP cationization also enhances the scale-up production of surface-modified NPs and prevents aggregation. However, there is still no attempt to use this method to modify cationic Au or HG coating to enhance drug loading capacity. Inspired by the great potential of using the AER-assisted method to functionalize Au and HG coating with cations, we hypothesized that a higher portion of SPIO@Au surface would be functionalized with SH-PEG-Py and PCC, thus resulting in higher stability and more loading sites for drug molecules (Fig. 1). To test our hypothesis, we have synthesized and innovatively improved the stability and loading sites by modifying the functionalization process of SPIO@Au NPs with SH-PEG-Py ligands using AER as assistants for surface-exchange reactions, denoted as SPIO@ Au-Py-PCC. PCC itself cannot be directly functionalized to SPIO@Au surface. Therefore, we used SH-PEG-Py NPs as a connecting bridge between SPIO@Au NPs and PCC. Being decorated with more SH-PEG-Py ligands, more cationic PCC cages could be anchored onto SPIO@Au NPs via the encapsulation of Py ligand as a guest molecule into the inner cavities of PCC. The strong hydrophobic inner cavities of PCC enhance the encapsulation of guest molecules through hydrophobic interactions, which was reported in our previous work [33]. The functionalization with PCC could improve the stability of MPNPs with higher surface charge and thus increase the loading rate of RA. In vitro drug release experiments were carried out through a 10-min periodic stimulation using a 100 mW LASER pointer (525 nm) as an irradiation source to demonstrate the on-demand release of RA under light stimulation. The release rate of RA was tested to be ~88\% after only 24 h with the periodically applied LASER. Cytotoxicity study has proved that SPIO@Au-Py-PCC NPs have minimal toxicity when introduced to PC-12 cells. To expand the scope of this method, the AER-assisted method was also applied to the newly reported SPIO@ hollow gold nanoshell (SPIO@HG) NPs [25] and thus demonstrated its versatility. The stability and surface charge of as-synthesized MPNPs could be pushed even higher with functionalization by MUTAB (11-mercapto undecyl-N, N, N-trimethylammonium bromide), a cationic surfactant.

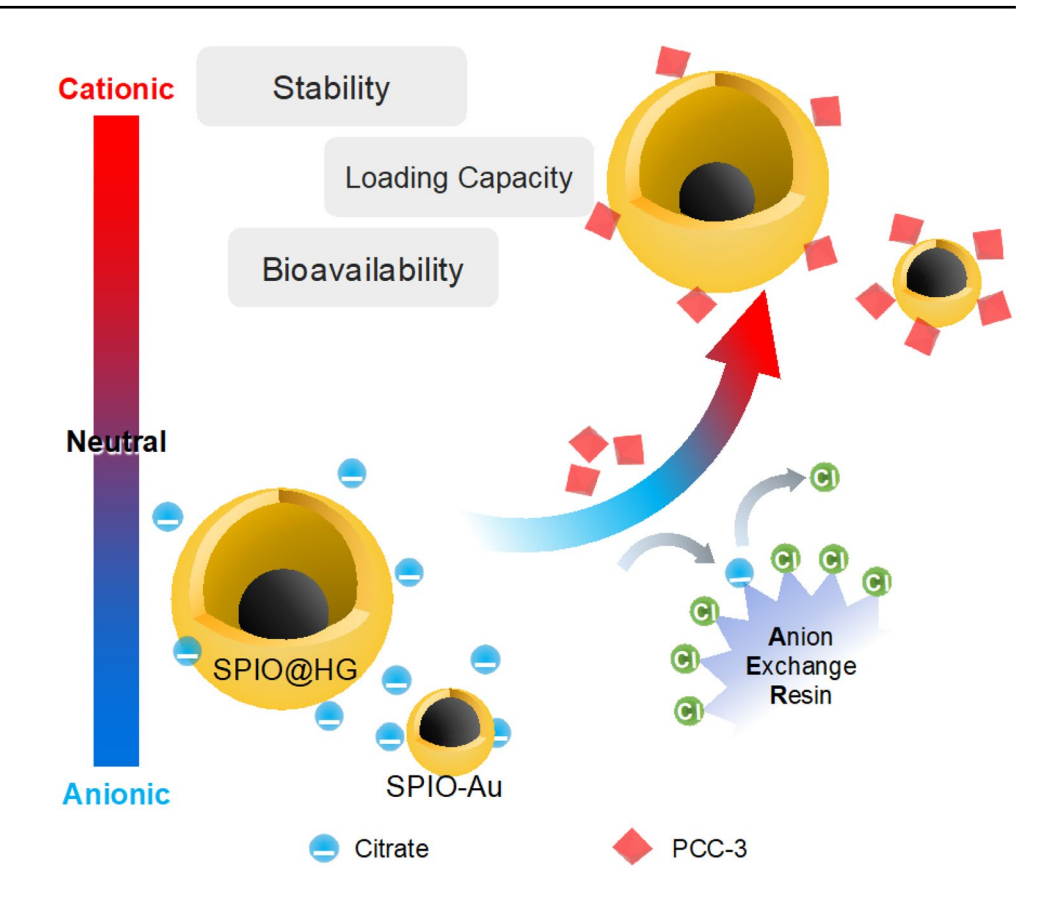
# 2 Experimental

#### 2.1 Materials

The chemicals below were obtained from corresponding manufacturers and used as received. SPIO NPs (EMG



Fig. 1 Schematic illustration of using the AER method to improve PCCs decorated SPIO@Au and SPIO-HG NPs



304, Ferrotec, Santa Clara, CA), trisodium citrate (Na<sub>3</sub>C<sub>6</sub>H<sub>5</sub>O<sub>7</sub>, 99%, Alfa Aesar, Haverhill, MA), chloroauric acid (HAuCl<sub>4</sub>, > 99.0%, Sigma-Aldrich, St. Louis, MO), Amberlite IRA-410 chloride form anion exchange resin (Sigma-Aldrich, St. Louis, MO), ammonium acetate (Sigma-Aldrich, St. Louis, MO), and SH-PEG-Py (PG2-PNTH-2 K, Nanocs, New York, NY). Cationic PCCs were prepared with reported methods (supporting information (SI)).

#### 2.2 Cell culture

PC-12 cells (ATCC, Manassas, VA) were cultured in RPMI-1640 Media with ATCC modification (Life Technologies, Carlsbad, CA) containing dilutions of 10% HI Horse Serum (Gibco, Thermo Fisher Scientific), 5% HI FBS (Gibco, Thermo Fisher Scientific, Waltham, MA), and 1% Penicillin Streptomycin (Gibco, Thermo Fisher Scientific, Waltham, MA). Materials included collagen from the human placenta, Bornstein and Traub Type IV, BioReagent (Sigma-Aldrich, St. Louis, MO), staining with SYTO-59 (Invitrogen, Thermo Fisher Scientific, Waltham, MA), staining with SYTOX Green (Invitrogen, Thermo Fisher Scientific, Waltham, MA), washing with 1×Hyclone PBS (Cytiva, Marlborough, MA), and dissociation with TrypLE (Gibco, Thermo Fisher Scientific, Waltham, MA).

# 2.3 Synthesis of SPIO@Au and SPIO@HG NPs

Synthesis of SPIO@Au NPs was based on a previously reported method [34]. In brief, commercial SPIO NPs were used as cores, and the gold coating was achieved on SPIO NPs with hydroxylamine as the reductant. SPIO NPs in aqueous suspension were mixed with sodium citrate and diluted using deionized (DI) water under mechanical stirring. Hydroxylamine and HAuCl<sub>4</sub> were then added sequentially to form the Au coating. After the color changed from brown to pink-red in 10 min, the resulting products were washed three times with DI water and then directly used for nextstep experiments without further treatments. Synthesis of SPIO@HG NPs was based on a previously reported method [25]. In brief, commercial SPIO NPs were used as cores, and the silver coating was synthesized on SPIO NPs first and then replaced by HAuCl<sub>4</sub> to form a hollow gold coating. In the end, SPIO@HG NPs were separated by centrifuging and rinsed with sodium citrate solution four times to remove the uncoated SPIO. The SPIO@HG NPs were then redispersed in sodium citrate solution (1.2 mmol) and used for next-step experiments without further treatment.



# 2.4 Functionalization of SPIO@Au or SPIO@HG NPs with SH-PEG-Py and PCC via direct exchange (DE) method

SPIO@Au NPs (or SPIO@HG) were functionalized firstly with SH-PEG-Py by suspending 1000 µg of corresponding NPs in 1 mL of DI water with 1500 µg of SH-PEG-Py and shaking on a shaker at room temperature for 24 h. Then, the SH-PEG-Py functionalized SPIO@Au (or SPIO@HG) NPs (SPIO@Au-Py or SPIO@HG-Py, respectively) were centrifuged and washed three times with DI water. After that, SPIO@Au-Py (or SPIO@HG-Py) NPs were suspended in 1 mL of DI water and mixed with 450 µg of cationic PCC at room temperature for 24 h, followed by centrifuging and washing process three times with DI water.

# 2.5 Functionalization of SPIO@Au NPs or SPIO@ HG NPs with SH-PEG-Py and PCC-3 via AER-assisted method

SPIO@Au NPs (or SPIO@HG) were functionalized firstly with SH-PEG-Py by suspending 1000  $\mu g$  of SPIO@Au NPs (or SPIO@HG) and 1.667 g of AER in 1 mL of DI water with 1500  $\mu g$  of SH-PEG-Py under ultra-sonication for better mixing and shaking on a shaker at room temperature for 2 h. The solution was taken out first to remove the AER beads. Then, the SH-PEG-Py functionalized SPIO@Au NPs (or SPIO@HG) (named as SPIO@Au-Py or SPIO@HG-Py) were centrifuged and washed three times with DI water. After that, SPIO@Au-Py NPs were suspended in 1 mL of DI water and mixed with 450  $\mu g$  of PCC at room temperature for 24 h, followed by centrifuging and washing process three times with DI water. The as-synthesized MPNPs were denoted as SPIO@Au-Py-PCC (or SPIO@HG-Py-PCC) NPs.

# 2.6 Functionalization of SPIO@HG-Py-PCC NPs with MUTAB via AER-assisted method

The as-synthesized SPIO@ HG-Py-PCC NPs were functionalized by MUTAB (11-mercapto undecyl-N, N, N-trimethylammonium bromide) by firstly suspending 1000  $\mu g$  of SPIO@HG-Py-PCC NPs and 1.667 g of AER in 1 mL of DI water with 1500  $\mu g$  of MUTAB under ultra-sonication for better mixing and shaking on a shaker at room temperature for 2 h. The solution was taken out to remove the AER bead. Then, the MUTAB functionalized SPIO@HG-Py-PCC NPs were centrifuged and washed three times with DI water.

#### 2.7 Characterizations

TEM analysis was performed on a Tecnai G2 F20 ST FE-TEM (FEI) at an operating voltage of 200 kV. Briefly, 20  $\mu$ L of each sample was dropped onto a 400-mesh copper grid (Electron Microscopy Sciences, Hatfield, PA) and left dry in the air. The light absorbance spectra of SPIO@Au and SPIO@HG were measured on a Hitachi U-4100 UV-Vis-NIR spectrophotometer. In addition, the  $\zeta$ -potential and the hydrodynamic diameter of SPIO@Au NPs with different functionalizations were measured with a Malvern Zetasizer Nano ZS (Malvern Instruments Inc.) equipment.

#### 2.8 Elemental analysis

The SPIO@Au NPs before and after functionalization with PCCs were digested in aqua regia. In detail, the NPs were dissolved by a mixture of concentrated hydrochloric acid (0.3 mL, ~30%) and concentrated nitric acid (1.1 mL, ~65%). The samples were diluted with 2% nitric acid and finally tested on the PerkinElmer NexION 300D ICP-MS (PerkinElmer, Inc.).

#### 2.9 Photothermal conversion evaluation

The same setup for the in vitro drug release was used to evaluate the photothermal conversion effect to reflect the real temperature change under in vitro experimental conditions. A GX3 high-power green LASER pointer was used as a light source (operation power: 100 mW). Slide-A-Lyzer<sup>TM</sup> MINI dialysis device kit (10 K MWCO, 0.1 mL) was used as the container. 1.2 mL of DI water and a mini stir bar were placed in the microcentrifuge tube, and a specific volume of SPIO@ Au-Py-PCC NPs with particular concentration was placed in the dialysis tube. A thermocouple (Omega, Stamford, CT, K-type, 0.076 mm wire diameter, and 0.33 mm bead diameter) was used to measure the temperature variation with time upon the LASER irradiation. A National Instruments NI9219 control system recorded the temperature variation curve with time. The stirring speed was set to 300 rpm. The LASER irradiation was started when the temperature had established equilibrium with room temperature. The LASER was turned off when the raised temperature stabilized.

# 2.10 Measurement of the drug loading efficiency

0.25 mg of SPIO@Au-Py-PCC NPs were mixed with 4  $\mu$ g of retinoic acid in 1.25 mL of DI water-methanol mixed solvent (v:v = 1:1). The tube was shaken under dark for 24 h. After the NPs were centrifuged and separated from the solvent, RA-loaded SPIO@Au-Py-PCC



NPs were obtained. The RA concentration before and after the loading process was measured using high-performance liquid chromatography (HPLC) described below. The payload was calculated based on the following equation:

$$Payload = \frac{Mass\ of\ RA\ loaded\ onto\ NPs}{Mass\ of\ NPs} \tag{1}$$

# 2.11 Determination of the in vitro drug release profile

The drug release profile of RA-loaded SPIO@Au-Py-PCC NPs was measured in DI water. The NPs were dispersed in 200  $\mu L$  of DI water and then introduced into a micro dialysis tube (10 K MWCO). The dialysis tube was then placed into a microcentrifuge tube containing 1.2 mL of DI water and a mini stir-bar. The stirring was set to 300 rpm during the release process to ensure an even temperature distribution in the liquids. The LASER light of 100 mW intensity was applied to the dialysis tube for 10 min between two consecutive time points. For time intervals longer than 6 h, the LASER was applied for three times in total. At each time point, all the released media were exchanged with fresh DI water. HPLC measured the clear solution with RA released within each time interval. The control group has no external light applied.

# 2.12 Analysis of RA using HPLC

RA was measured by HPLC (2030C, Shimadzu) equipped with a reversed-phase C18 column in the low-pressure gradient mode. A mixture of methanol and 10 mM ammonium acetate (75:25, v:v) was used as the mobile phase at a 1.0 mL·min<sup>-1</sup> flow rate. The column effluent was monitored using a UV detector set at 350 nm. RA stock solutions were prepared in methanol and then stocked in freezer under dark. Calibration curves were obtained from RA-methanol solutions over the range of 0.3 to 190  $\mu$ g/mL. The curve was linear, and  $R^2$  was 0.996.

# 2.13 Cell viability evaluation by flow cytometry

PC-12 cells were seeded into a 48-well plate pre-coated with collagen type IV. The cells were then incubated at 5% CO<sub>2</sub> and 37 °C. After 24 h, the cells were incubated with media containing SPIO@ Au-Py-PCC NPs at concentrations between 0 µg/mL and 40 µg/mL. After 1, 3, and 5 days, the media were aspirated, and the cells were stained with 200 µL of 5 µM SYTOX Green and SYTO-59 (1:1000 dilution from stock solution, Invitrogen) for 10 min. Cells were then observed and imaged using an EVOS<sup>TM</sup> microscope at  $10 \times$  magnification. The staining solution was removed, and

the cells were washed with PBS, treated with Tryp-LE for 10 min and then resuspended in media for flow cytometry measurement using a BD Accuri<sup>TM</sup> C6 flow cytometer equipped with a FL1 (553 nm) and FL4 detector. Viability data was acquired at a flow rate of 35  $\mu$ L·min<sup>-1</sup> with a minimum of 10.000 events detected.

#### 3 Results

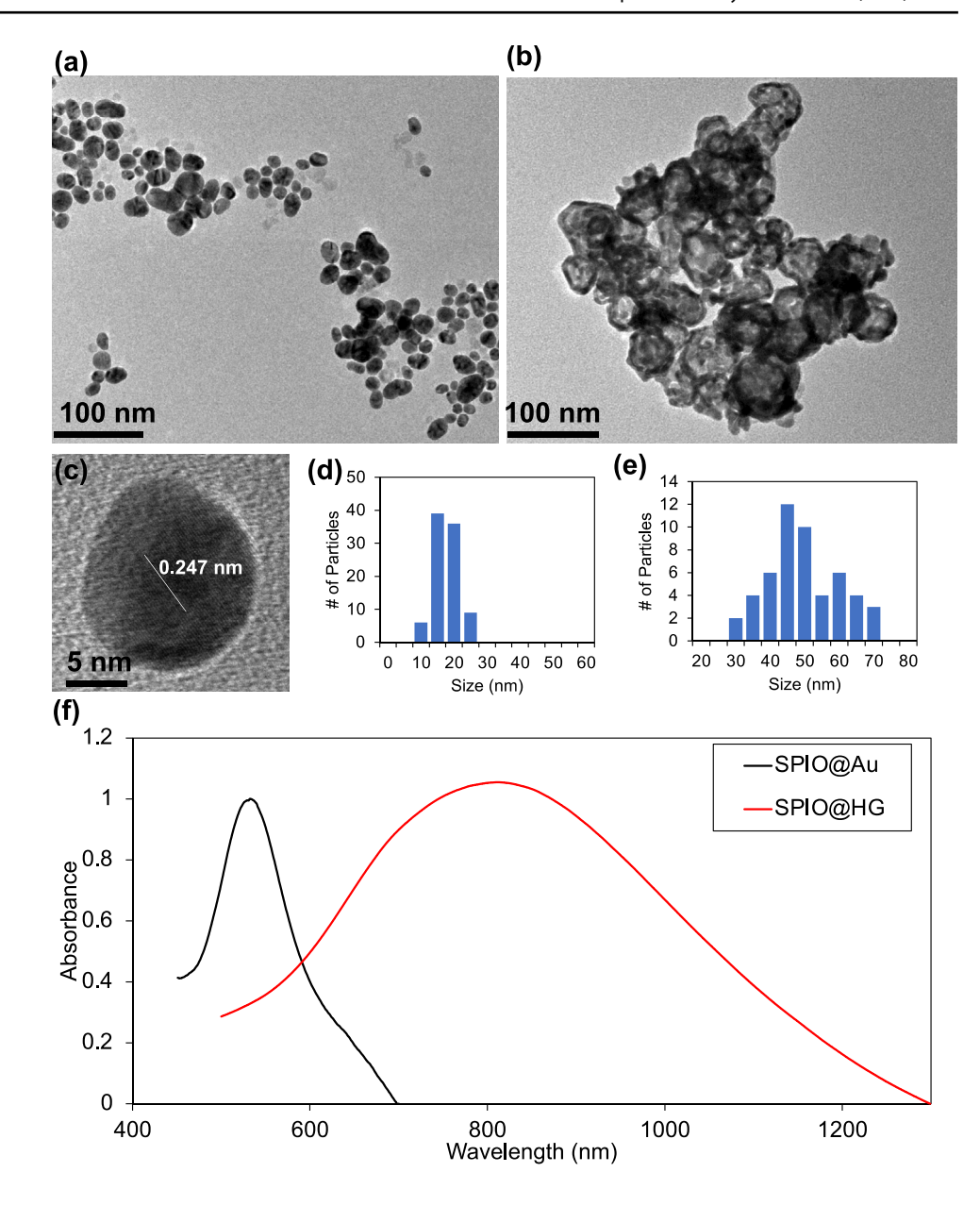
# 3.1 Characterization of functionalized NPs

In this nanocarrier system, SPIO cores confer magnetic targeting abilities to this nanocarrier. Au NPs enable light-triggered drug delivery under plasmonic heat. SH-PEG-Py molecules act as a connecting bridge between Au@SPIO NPs and PCC. PCC is the main drug encapsulating component, while it does not have the light stimulable ability and magnetic property, therefore requiring the combination with SPIO and Au. In this work, the synthesis of SPIO@Au NPs was carried out using the reported methods [34]. The functionalization of SPIO@ Au NPs was performed using an AER-assisted method, with SH-PEG-Py ligands being used as surface decorators. TEM images (Fig. 2a, c, and d) of SPIO@Au-Py-PCC NPs showed the SPIO@Au-Py-PCC NPs (D:  $19.5 \pm 3.6$  nm) with a quasispherical shape and a narrow size distribution. No aggregation was observed from TEM images. The lattice spacing of Au (0.247 nm) was confirmed. TEM images (Fig. 2b and e) of SPIO@HG NPs (D:  $52.0 \pm 10.5$  nm) showed a clear hollow gold shell structure. In addition, our previous work [25] have demonstrated the hollow core-shell structure through highresolution TEM, which confirmed the existence of both the SPIO and the wrapping HG using elemental mapping. We have also illustrated the uniform formation using high-resolution scanning electron microscopy (SEM) [25]. The light absorbance measurements (Fig. 2f) confirmed the SPR peak of SPIO@Au and SPIO@HG NPs at 532 nm and 812 nm.

To quantify the effect that the AER-assisted method brought, the ζ-potential and hydrodynamic diameters of NPs were tested. Effects of different usage of surface decorators were studied. Defining the NPs functionalized with a calculated stoichiometric dose of SH-PEG-Py prescribed as SPIO@ Au-Py-1, NPs decorated with 50% more (SPIO@Au-Py-1.5) and double doses (SPIO@Au-Py-2) were also prepared. As shown in Table 1(a), a significant change of surface charge was observed due to the functionalization with SH-PEG-Py: It jumped from –39.9 mV to 34.8 mV and 36.0 mV for SPIO@ Au-Py-1 and SPIO@Au-Py-1.5, respectively, indicating the high-efficiency replacement of surface citrates by SH-PEG-Py ligands. Compared to the hydrodynamic size (39.8 nm) of citrated SPIO@Au NPs, size of SPIO@Au-Py NPs was also expanded to 148.4 nm and 120.7 nm for SPIO@Au-Py-1 and



Fig. 2 a TEM images of SPIO@ Au-Py-PCC NPs. b TEM images of SPIO@ HG NPs. c Lattices of Au on SPIO@ Au-Py-PCC NPs. d Size distribution of SPIO@ Au-Py-PCC NPs. e Size distribution of SPIO@ HG NPs. f Light absorbance spectra of SPIO@ Au and SPIO@ HG NPs



SPIO@Au-Py-1.5, respectively, due to the expanding volume from the SH-PEG-Py ligands. However, the excessive amount of SH-PEG-Py was not favored as it caused a decrease in

 $\zeta$ -potential and an increased hydrodynamic size in the SPIO@ Au-Py-2 sample.

Table 1 ζ-Potentials and hydrodynamic diameters of SPIO@Au NPs with different functionalizations with AER

(a) Different dosage of SH-PEG-Py ligands								
NPs	SPIO@Au	SPIO@Au-Py-1	SPIO@Au-Py-1.5	SPIO@Au-Py-2				
ζ-potential (mV)	$-39.9 \pm 0.1$	$34.8 \pm 0.8$	$36.0 \pm 1.3$	$30.3 \pm 0.6$				
Hydrodynamic diameter (nm)	$39.8 \pm 3.5$	$148.4 \pm 1.5$	$120.7 \pm 1.7$	$257.0 \pm 5.4$				
(b) Different dosage of PCC ca	ages							
NPs	SPIO@Au-Py-1.5	SPIO@Au- Py-1.5-PCC-1	SPIO@Au- Py-1.5-PCC-1.5	SPIO@Au- Py-1.5-PCC-2				
ζ-potential (mV)	$36.0 \pm 1.3$	$29.1 \pm 2.0$	$38.9 \pm 0.7$	$40.0 \pm 1.1$				
Hydrodynamic diameter (nm)	$120.7 \pm 1.7$	$148.6 \pm 1.4$	$123.1 \pm 1.6$	118.6±0.7				



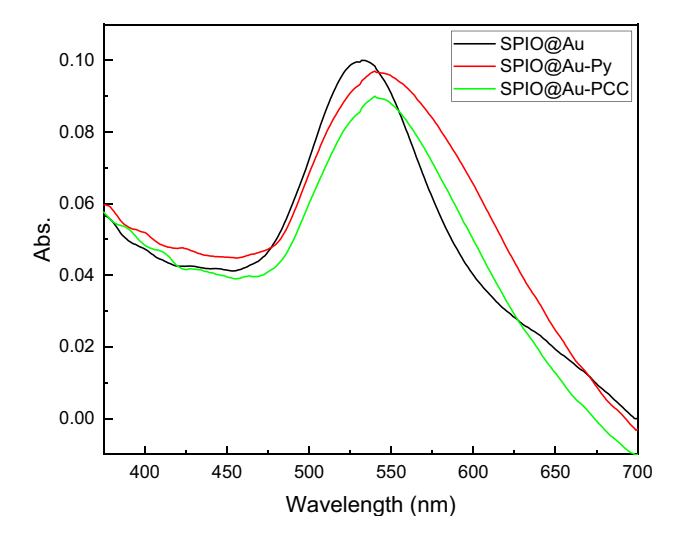


Fig. 3 UV-Vis spectra of SPIO@Au NPs before and after surface modification

Different dosages of PCC cages also had an impact on the outcomes (Table 1(b)). The highest surface charge (40.0 mV) and smallest hydrodynamic diameter (118.6 nm) were achieved on SPIO@Au-Py-1.5-PCC-2, indicating the highest stability. Notably, the results for SPIO@Au-Py-1.5-PCC-1.5 were also very close. Regarding the conservation and effective utilization of PCC cages, the condition of SPIO@Au-Py-1.5-PCC-1.5 was picked as the standard preparation procedure for drug carriers. To confirm the coating of PCC does not affect the optical property of SPIO@Au NPs, light absorbance spectra of SPIO@Au NPs before and after the conjugation with Py and PCC were measured and shown in Fig. 3. A slight shift in UV-Vis absorbance peak was observed after the conjugation with SH-PEG-Py ligands, indicating the effective binding between ligands and SPIO@Au NPs. No obvious difference was observed between SPIO@Au-Py and SPIO@ Au-Py-PCC, indicating the PCC conjugation did not affect the optical property of NPs.

To demonstrate the effectiveness and versatility of the AER-assisted method, both the SPIO@Au and the newly reported SPIO@HG NPs were functionalized with the SH-PEG-Py and cationic PCC cages in tandem with DE and AER-assisted surface exchange methods (Table 2). Preferred

**Table 3** Relative mass components of SPIO@Au (SPIO@HG) and SPIO@Au-Py-PCC (SPIO@HG-Py-PCC) NPs. Results were obtained from ICP-MS analysis

NPs	Method	Fe/%	Au/%	Pd/%
SPIO@Au	-	25.8	74.2	-
SPIO@Au-Py-PCC	DE	24.7	75.0	0.3
	AER-assisted	24.0	72.9	3.1
SPIO@HG	-	19.2	80.8	-
SPIO@HG-Py-PCC	AER-assisted	18.3	77.5	4.2

dosage was used for both NPs. As observed, the surface exchange proceeded by the DE method which has low exchange efficiency: The surface charge of both SPIO@Au and SPIO@HG NPs cannot cross the threshold of 0 mV, and the colloidal stability dropped as hydrodynamic diameter significantly increased. As a comparison, the AER method successfully "pushed" NPs to achieve higher surface charge and thus resulted in better aqueous stability. High surface charges (38.9 mV for SPIO@Au, 22.0 mV for SPIO@ HG NPs, respectively) and small hydrodynamic diameters (123.1 nm for SPIO@Au, 199.9 nm for SPIO@HG NPs, respectively) were both observed in NPs treated by AER method. We observed a difference between TEM-measured size and hydrodynamic diameter. This is possibly due to the polydispersity and shape irregularity, as intrinsic properties of large-size MNPs with 20 nm diameter and above [35]. Another reason is the magnetic dipole–dipole interactions between NPs which may cause their agglomeration even without a magnetic field [36].

To better understand the components of functionalized SPIO@Au and SPIO@HG NPs, element analysis was performed (Table 3). In this nanocarrier system, the concentration of Au reflects the concentration of Au shell (solid gold or hollow gold) as the plasmonic component, and the concentration of Fe reflects the concentration of SPIO core (Fe<sub>3</sub>O<sub>4</sub>) as the magnetic component. Pd concentration reflects PCC cages' concentration as the main drug carrier component (Pd as an element of PCC's building units). The mass ratio between Au and Fe remained the same (Au: Fe = 3:1 for SPIO@Au, 4:1 in SPIO@HG) before and after the surface functionalization. The high mass

Table 2 Comparison of colloidal stability of SPIO@Au and SPIO@HG NPs with different surface functionalization methods

Functionalization	Original	With Py (DE)	With Py (AER)	With Py (DE)-PCC	With Py (AER)-PCC
(a) SPIO@Au NPs					_
ζ-potential (mV)	$-39.9 \pm 0.1$	$-35.4 \pm 0.7$	$36.0 \pm 1.3$	$-16.9 \pm 4.6$	$38.9 \pm 0.7$
Hydrodynamic diameter (nm) (b) SPIO@HG NPs	$39.8 \pm 3.5$	$184.6 \pm 9.4$	$120.7 \pm 1.7$	$281.7 \pm 23.1$	$123.1 \pm 1.6$
ζ-potential (mV) Hydrodynamic diameter (nm)	$-44.5 \pm 1.4$ 211.8 ± 14.3	$-24.8 \pm 0.6$ $180.9 \pm 4.7$	$7.0 \pm 1.0$ $376.4 \pm 24.5$	$-13.9 \pm 1.0$ $1273.7 \pm 39.4$	$22.0 \pm 0.5$ $199.9 \pm 3.2$



ratio of Pd (3.1% for SPIO@Au-Py-PCC, 4.2% for SPIO@ HG-Py-PCC) proved the successful and efficient decoration of PCC-3 cages onto MPNPs. Based on the molar ratio of 6:1 for Pd to PCC, we estimated the number of PCCs per SPIO@Au to be 310 per NP. Compared to the elemental analysis of NPs functionalized by the DE method, the improvement in the mass rate of PCC-3 was significant (310 compared to 30), which met our needs for more functionalized drug-loading units.

To further improve the stability of SPIO@HG-Pv-PCC NPs, we used a second cationic surfactant MUTAB to increase the surface charge to a higher level. Due to the competition between SH-PEG-Py ligands and MUTAB ligands, the sequential effect was studied (Fig. 4). When various ligands, including SH-PEG-Py, PCC, and MUTAB, were sequentially functionalized onto SPIO@HG NPs, the order of functionalization had a distinct impact on the resulting surface characteristics, as assessed by  $\zeta$ -potential and hydrodynamic diameter measurements. For example, the sequence starting with SH-PEG-Py, followed by PCC, and then MUTAB, yielded the highest colloidal stability with the highest surface charge of 30.3 mV and the smallest hydrodynamic diameter of 160.8 nm. In an alternate approach where MUTAB was functionalized first, followed by SH-PEG-Py and PCC, the final product's measured surface charge and hydrodynamic diameter were 24 mV and 186.8 nm, respectively. In the final approach, combining SH-PEG-Py and PCC initially, followed by functionalization with SH-PEG-Py-PCC onto SPIO@HG NPs, resulted in a final product with the lowest  $\zeta$ -potential of -6.0 mV and the largest hydrodynamic diameter of 1069 nm, indicating the reduced colloidal stability compared to the first two cases.

The critical problem we aim to solve is the improvement of the functionalization efficiency of SPIO@Au and SPIO@ HG NPs. Both NPs were initially synthesized with protection by anionic citrates to achieve a uniform size distribution. Since cationic PCC functionalization is required for drug loading, turning anionic SPIO@Au NPs to cationic smoothly is challenging. The DE method, which can be realized by simply mixing the citrate-stabilized NPs with cationic ligands, will have to raise the surface charge to neutral, which leads to severe and irreversible aggregation and should be avoided. The directly synthesized SPIO@Au-Py-PCC NPs cannot pass the threshold of 0 mV even with excessive SH-Py-PEG ligands and PCC cages being used. The estimated number of PCC cages decorated on each NP could have been higher and thus limits the loading capacity. Besides that, the near-neutral surface charge also harms the stability and bioavailability. Recently, Yonezawa et al. reported a rapid and efficient surface exchange of citrate-protect Au NPs with cationic thiol ligands under the

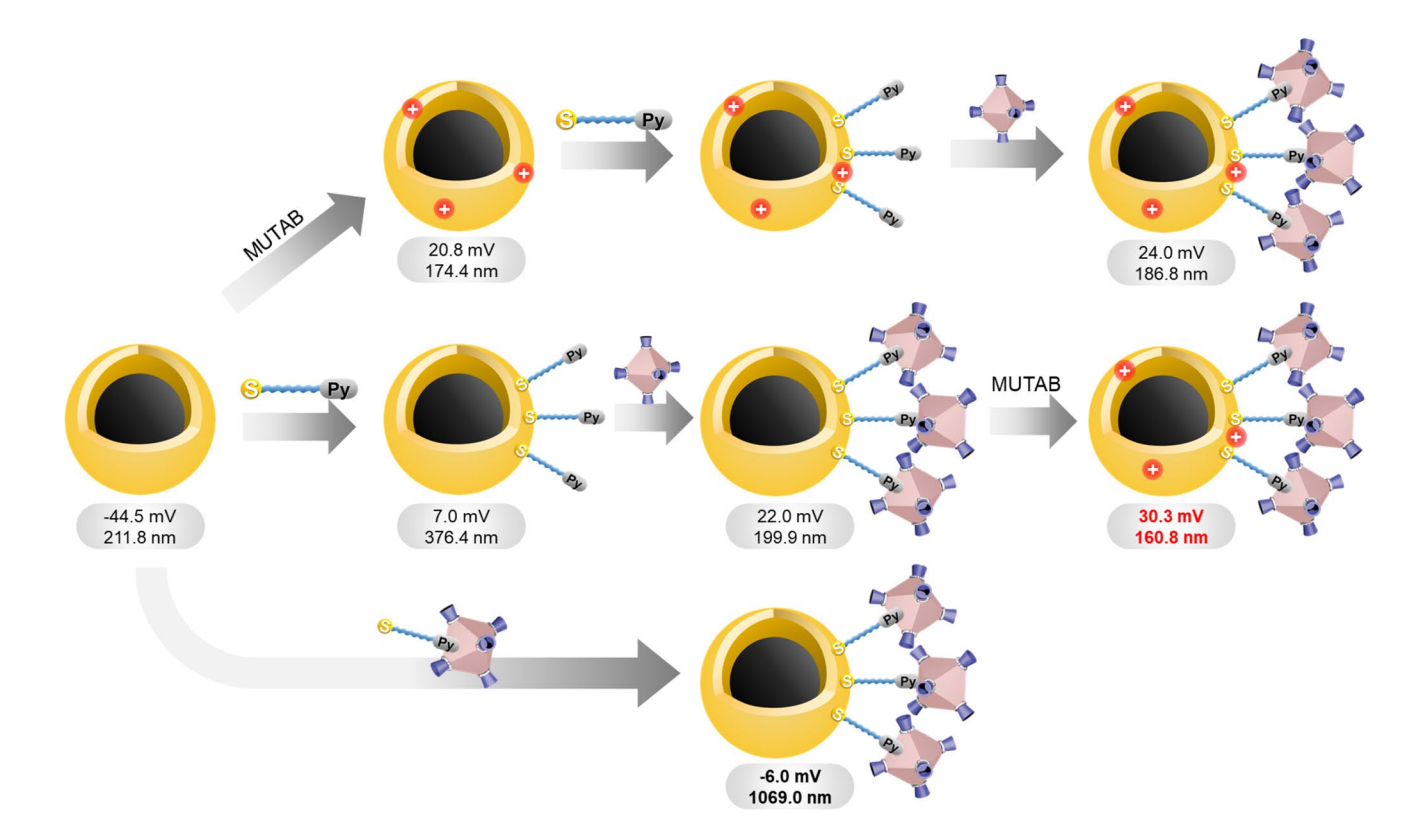


Fig. 4 Sequential effect of functionalization by different ligands. Up: functionalize with MUTAB first and then SH-PEG-Py and PCC. Middle: functionalize with SH-PEG-Py and PCC first and then MUTAB. Down: Functionalize with already-complexed SH-PEG-Py-PCC molecules



presence of AER in a water [32]. The AER absorbed the citrates that have been replaced from the surface of Au, pushing the exchange reaction forward to a complete end as removing products (citrates) from the reactants makes the replacement direction thermodynamically favored. The kinetics of this method were also reported to be very fast, as only 20 min were required to complete the surface exchange process.

In our work, with the help of AER, the efficiency of surface functionalization of SPIO@Au NPs was greatly improved. The highest surface charge achieved was  $39.97 \pm 1.07$  mV for SPIO@Au-Py-1.5-PCC-2, which was far higher than the surface potential of NPs functionalized through the DE method ( $-16.9 \pm 4.6$  mV). The relatively small hydrodynamic size of as-functionalized NPs ( $118.60 \pm 0.73$  nm) also demonstrated good aqueous stability and potentially excellent bioavailability [37]. The elemental analysis results (10.2% of Pd's mass rate) further indicated much higher (compared to the previous 0.3% mass rate of Pd) numbers of PCC functionalized to NPs, suggesting the success of complete surface decoration.

#### 3.2 Photothermal conversion

The photothermal conversion effect is essential in a controlled drug release from carriers. To examine the photothermal response of SPIO@Au-Py-PCC NPs for a better understanding of their behavior in situ, the measurement was performed in the same apparatus for the in vitro release study (Fig. 5a). The incident wavelength of LASER was set to 525 nm to match the SPR peak of SPIO@Au. The power of incident LASER was set to be 100 mW.

The temperature profile of SPIO@Au NPs with different concentrations from 100 to 1000  $\mu g \cdot m L^{-1}$  was measured first (Fig. 5b). As shown in the results, the LASER caused a higher temperature to rise around 10.6 °C after 10.5 min when the concentration of NPs was 200  $\mu g/mL$ , compared to the case of NPs at 100  $\mu g/mL$ . However, NPs of higher

concentrations (500 µg/mL, 1000 µg/mL) achieved lower temperature rise (4.7 °C, and 5.3 °C, respectively). This lower temperature rise is possible because, at higher concentrations, the NPs quench most of the LASER light at the beginning of the light path through the NPs' solution. Thus, the LASER cannot reach all the NPs efficiently. These results suggest that even though a higher concentration of NPs may carry more drugs, it will drastically reduce the depth the LASER can penetrate and cause a much weaker overall heating effect.

In the next step, the optimal concentration of 200  $\mu$ g/mL was used to measure the temperature profile of SPIO@ Au NPs with different volumes (Fig. 5c). The measured thermal variation curves showed that a lower maximum temperature rise was achieved for larger volumes of NPs. This increasing heat dissipation was due to the larger liquid volume. However, the temperature increases of 16 °C for 100  $\mu$ L liquid was too high for drug delivery and on-demand treatment purposes in biological applications. Thus, 200 uL was selected as the optimal volume for in vitro cell-free drug release study due to the moderate temperature rise (7.9 °C).

# 3.3 Drug loading and in vitro cell-free release study

The drug loading capacity of SPIO@Au-Py-PCC is hypothesized to be improved with the assistance of AER because of the following reasons: (a) more PCC cages were anchored onto NPs when more surface area was functionalized with SH-PEG-Py ligand using AER; (b) the host–guest interaction between hydrophobic PCC cages and hydrophobic retinoic acid enables the loading of RA into PCC-3; (c) the high positive charge of NPs also promotes the loading as retinoic acids can partially ionize into anions and thus being attracted by the NPs.

The loading rate of RA was determined by measuring the concentration difference of RA solution before and after the loading by HPLC. As a result, the RA's loading rate was

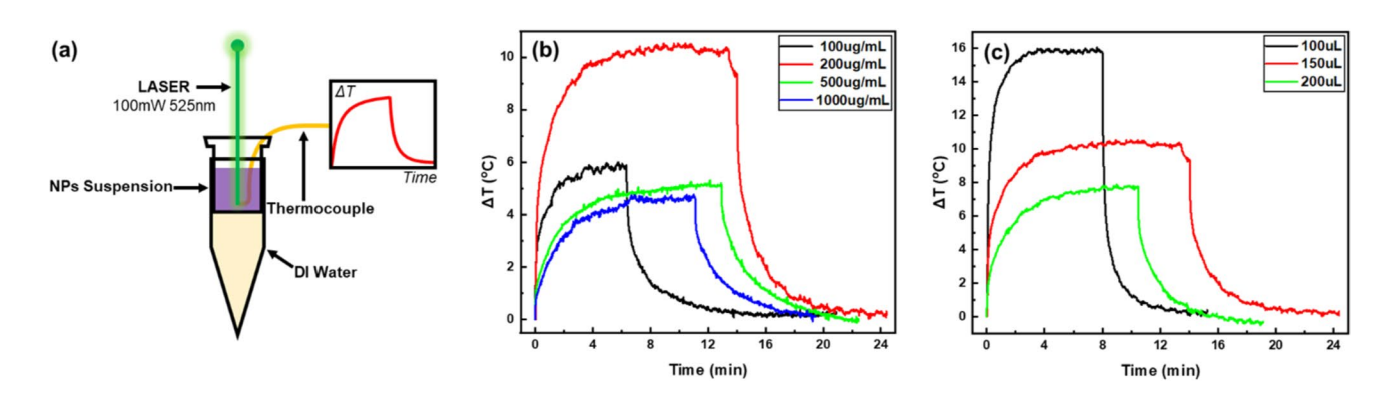


**Fig. 5 a** Experimental setup of the temperature measurement of SPIO@Au NPs solutions. **b** The temperature profile of SPIO@Au NPs in DI water with different concentrations. (Volume is set to be

150  $\mu$ L,) c Temperature profile of SPIO@Au NPs with different volumes. (Concentration is set to be 200  $\mu$ g·mL<sup>-1</sup>.)



determined to be 32.29  $\mu$ g/mg NPs. This demonstrated that the AER-assisted method could lead to a much higher RA loading capacity than the DE method (13.51  $\mu$ g/mg NPs).

The in vitro release of RA from RA-loaded SPIO@Au-Py-PCC NPs was then measured. When taking samples, a dialysis tube was used to help separate the released drug from the NP solution. 200  $\mu L$  of 200  $\mu g/mL$  SPIO@Au-Py-PCC NPs (calculated based on SPIO@Au) was loaded into the dialysis tube, with 1.2 mL of DI water loaded as a solvent in the tube. After each period, the solvent with released RA in the dialysis tube was collected for analysis; the tube was then refilled with fresh DI water to start the subsequent illumination by LASER (Fig. 6a). The light group was irradiated by 100 mW 525 nm LASER for 10 min at each time interval (three times for more extended periods), while the control group remained untreated.

The cumulative RA release profile from SPIO@Au-Py-PCC NPs showed a significant difference between the light and control groups (Fig. 6b). Around 87.9% of loaded RA was released after 24 h, much higher than the 54.8% release rate in the control group. Being extended to 72 h, around 97.6% of RA was released in the light group, while more than 40% of RA remained unreleased without LASER treatment.

The initial stage of the RA release profile from SPIO@ Au-Py-PCC NPs was also measured to help understand the kinetical behaviors (Fig. 6c). The initial release rate remained low and steady in the first 3 h, with an acceleration occurring afterward. Such a delayed release could be

attributed to the size effect of RA and strong interactions between the PCC-3 cages and RA molecules.

A higher loading rate of RA was demanded to reduce the cost of materials and the potential toxicity to cells caused by increased dosage of NPs. This can be achieved from the higher loading number of PCC cages, which contributed to a higher level of interaction between hydrophobic inner cavities of PCC cages and hydrophobic RA molecules. The higher positive charge of NPs also promoted the Coulombic attraction between cationic NPs and anions dissociated from RA molecules. Compared to the previously reported payload (13.51 µg/mg), a 139% improvement was observed, proving this methodology's efficacy. In addition, RA's short half-life and rapid metabolization process require a controlled and sustained release pattern over time [38]. Literature reported the use of gliadin NPs [39] and polyethyleneimine-dextran sulfate NPs [38] with payloads of 76 and 86 ug RA/ mg NPs, respectively. While their NPs exhibit a higher payload, these NPs either lack prolonged release capacities or do not offer controlled release triggered by external stimuli. Previous studies have explored other approaches for light-controlled drug release. For instance, Bozuyuk et al. reported a work utilizing 3D-printed magnetic chitosan microswimmers for the light-triggered release of doxorubicin [40]. This drug carrier exhibited a rapid drug release pattern, with most of the payload released within 5 min. Luo et al. conducted another work using liposomes as carriers of doxorubicin [41]. Under laser illumination,

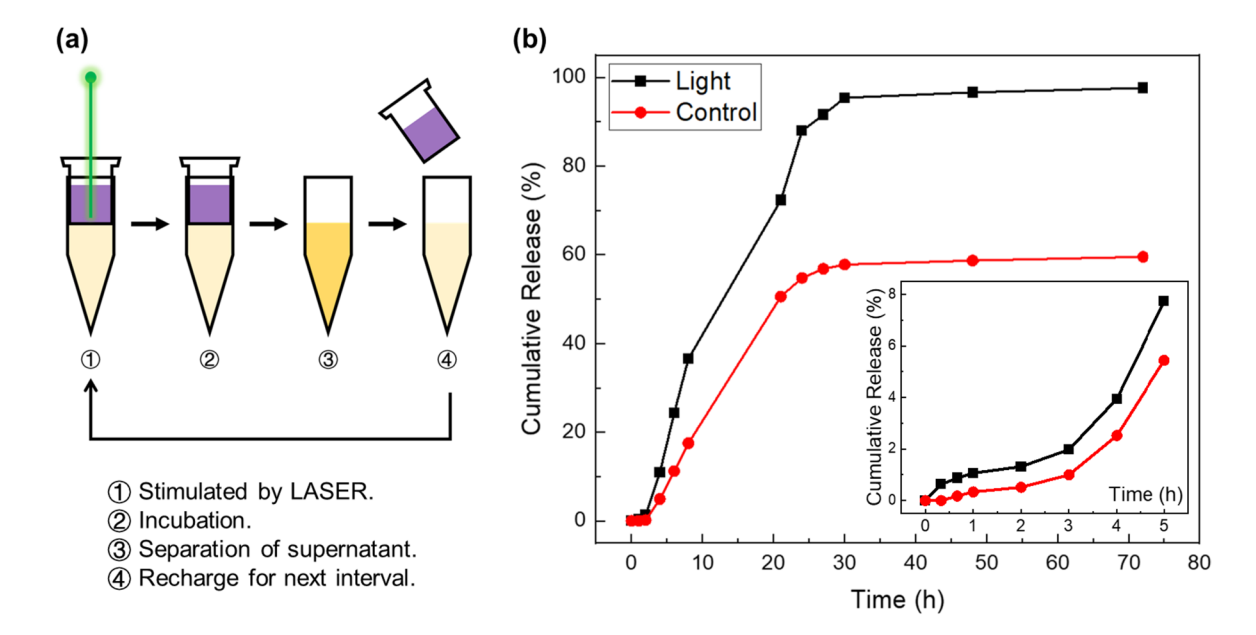


**Fig. 6** a Experimental procedure for in vitro drug release: ① treated by a laser pointer for 10-min period; ② incubate until the end of time interval; ③ collect supernatant for analysis of released RA; ④ recharge the tube with fresh DI water for the subsequent treatment. **b** The

cumulative release profile of RA in DI water from SPIO@Au-Py-PCC NPs (200  $\mu$ L, 200  $\mu$ g/mL). Inset: initial release profile of RA in DI water from SPIO@Au-Py-PCC NPs (500  $\mu$ L, 200  $\mu$ g/mL)



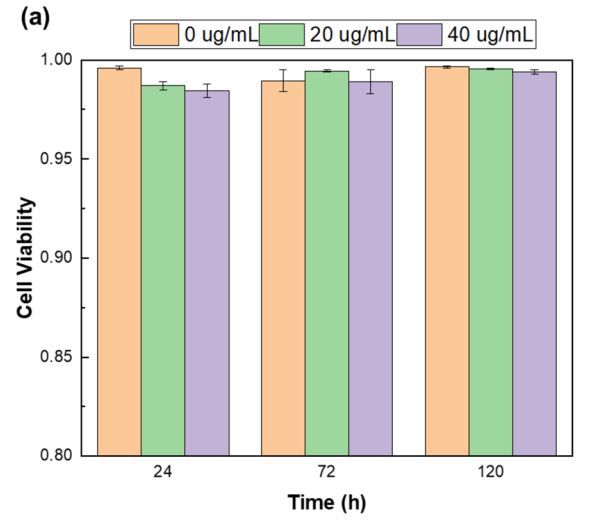
the drug was released in 100% within 5 min. Compared to these light-triggered drug release strategies characterized by their fast-release kinetics, our nanocarrier demonstrates a sustained and prolonged release of RA for over 30 h. Therefore, this nanocarrier has the strong potential to enhance the in vivo efficiency of RA delivery.

Furthermore, the magnetic core of this nanocarrier not only improves the cellular uptake [42], but also indicates its potential for magnetic-field-guided delivery to the targeted site [27]. Nonetheless, a main obstacle that hinders the practical application of this nanocarrier is the relatively small size of the SPIO core (< 10 nm) with limited magnetic response in vivo. In the future, we will develop SPIO cores with varying sizes, morphology, and shapes, such as nanorods, to enhance their magnetic properties. Additionally, MPNPs can be co-printed with biodegradable hydrogel for sustainable and targeted drug delivery. For example, the embedment of MPNPs with 3D-printed microrobots can substantially enhance their targeting ability by modulating the swimming behavior [43]. Moreover, the surfacemodified SPIO@Au NPs as functional fillers can also be combined with electromagnetic composites [44–47], such as carbon nanotubes/epoxy nanocomposites and polystyrene/ graphene composites. Epsilon near-zero properties from nanocomposites can be combined with MPNPs to develop multi-modal therapeutic agents.

Furthermore, we evaluated the photothermal conversion and the drug release study on SPIO@Au NPs but not SPIO@HG. The reason is that SPIO@HG is not at its optimal design that can cross BBB at its best efficiency due to the less saturation magnetization than SPIO@Au NPs [28]. Future work will be focused on modifying the structure of SPIO@HG to obtain higher saturation magnetization and to enhance the BBB crossing efficiency under a MF, which is not the focus of this paper.

# 3.4 Cellular toxicity study

To determine the impact of SPIO@Au-Py-PCC on in-vitro cell viability, PC-12 cells were treated with NPs at concentrations between 0 µg/mL and 40 µg/mL. For up to 5 days of incubation, cell viability was unaffected. There was no significant decrease in the live-to-total cell ratio for all NPtreated groups compared to the control group. This indicates that SPIO@Au-Py-PCC NPs, at all mentioned concentrations, do not induce significant toxic effects on PC-12 cells (Fig. 7a). In addition, the cell viability results in SPIO@ HG-Py-PCC NPs also showed minimal toxicity of these NPs on PC-12 cells (Fig. 7b). The results indicated a high level of biocompatibility for both the surface-modified SPIO@ Au-Py-PCC and SPIO@HG-Py-PCC NPs at the concentration of 40 µg/mL. However, we did not assess the toxicity at higher concentrations, such as 100 µg/mL and 200 µg/ mL, due to the significant temperature increase observed at these concentrations under laser illumination (> 10 °C). Such elevated temperatures are not suitable for cellular and animal studies. Also our previous work reported a slight toxicity at and above a concentration of 80 µg/mL [23]. Therefore, we consider SPIO@Au-Py-PCC at a concentration of 40 µg/mL safe for cellular evaluations. Moreover, existing literature has reported investigations into the in vivo toxicity of similar NPs, such as Au NPs with PEG coating. The previous results proved that PEG-coated Au NPs at the size of 20 nm had no obvious toxicity compared to the larger size of NPs at the dosage of 4 mg/kg for 28 days [48]. These results provide additional support for the safety of our NPs in biological



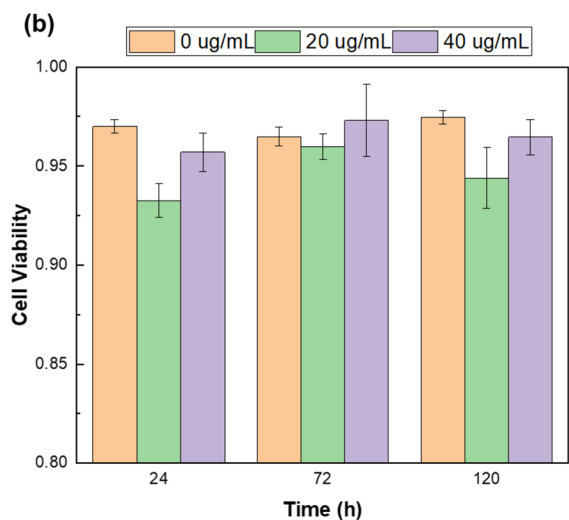


Fig. 7 Cell viability was measured from flow cytometry for PC-12 cells treated with different concentrations of a SPIO@Au-Py-PCC NPs; b SPIO@HG-Py-PCC NPs. Cells without treatment by NPs were used as the control group



applications. In future animal studies, we will further explore the acute and sub-acute toxicity of SPIO@Au-Py-PCC NPs under different dosages.

#### 4 Conclusions

To summarize, we have presented a highly effective approach for constructing drug loading units-enriched smart nanocarriers from PCCs and SPIO@Au NPs with the assistance of AER. The TEM images revealed the size and morphology of NPs. The notably high positive ζ-potential values and small hydrodynamic diameters indicated the successful modification of SPIO@Au NPs and their outstanding colloidal stability. This nanocarrier achieves a remarkably high payload of 32.39 µg/mL. The sustained and prolonged release for over 30 h was observed under periodically applied LASER light source, suggesting their potential for on-demand drug delivery. The cell viability results confirmed the high biocompatibility of these as-synthesized nanocarriers. In brief, our findings demonstrated that the as-synthesized drug carriers possess several key features: high positive charge, exceptional colloidal stability, excellent photothermal response, and minimal toxicity, which suggest their substantial potential for neuro-regenerative drug delivery.

**Supplementary Information** The online version contains supplementary material available at https://doi.org/10.1007/s42114-023-00811-4.

**Acknowledgements** The authors would like to thank the Material Characterization Facility at Texas A&M University for the help in this work.

Authors' contributions The manuscript was written through the contributions of all authors. Material preparation, data collection, and analysis were performed by T-HY, MY, NN, JC, XF, TF, MCH, and ZX. The first draft of the manuscript was written by T-HY and MY. YL, J-PP, H-CZ, and YW commented and revised on previous versions of the manuscript. All authors read and approved the final version of the manuscript. MY and T-HY contributed equally.

**Funding** This work was kindly supported by the United States National Science Foundation (Award # CMMI 1851635, Y.W.; Award # ECCS 2021081, Y.W. and Y.L.). This work was also supported by the award R01GM110137 (J.-P.P.) from the US National Institute of General Medical Sciences.

**Availability of data and material** The datasets generated during and/or analyzed during the current study are available from the corresponding author upon reasonable request.

#### **Declarations**

Competing interests The authors declare no competing interests.

Conflict of interest The authors declare no competing interests.

#### References

- Marras C, Beck JC, Bower JH, Roberts E, Ritz B, Ross GW, Abbott RD, Savica R, Van Den Eeden SK, Willis AW, Tanner C (2018) Prevalence of Parkinson's disease across North America. NPJ Parkinson's Disease 4
- Wohlfart S, Gelperina S, Kreuter J (2012) Transport of drugs across the blood-brain barrier by nanoparticles. J Control Release 161:264–273
- Esteves M, Cristóvão AC, Saraiva T, Rocha SM, Baltazar G, Ferreira L, Bernardino L (2015) Retinoic acid-loaded polymeric nanoparticles induce neuroprotection in a mouse model for Parkinson's disease. Front Aging Neurosci 7
- Wu H, Zhao J, Fu B, Yin S, Song C, Zhang J, Zhao S, Zhang Y (2017) Retinoic acid-induced upregulation of miR-219 promotes the differentiation of embryonic stem cells into neural cells. Cell Death Dis 8:e2953
- Hu J, Liu Y-F, Wu C-F, Xu F, Shen Z-X, Zhu Y-M, Li J-M, Tang W, Zhao W-L, Wu W, Sun H-P, Chen Q-S, Chen B, Zhou G-B, Zelent A, Waxman S, Wang Z-Y, Chen S-J, Chen Z (2009) Longterm efficacy and safety of all-trans retinoic acid/arsenic trioxidebased therapy in newly diagnosed acute promyelocytic leukemia. Proc Natl Acad Sci 106:3342–3347
- Ferreira R, Napoli J, Enver T, Bernardino L, Ferreira L (2020) Advances and challenges in retinoid delivery systems in regenerative and therapeutic medicine. Nat Commun 11
- Szuts EZ, Harosi FI (1991) Solubility of retinoids in water. Arch Biochem Biophys 287:297–304
- Huang Y, Zhang B, Xie S, Yang B, Xu Q, Tan J (2016) Superparamagnetic Iron oxide nanoparticles modified with tween 80 pass through the intact blood–brain barrier in rats under magnetic field. ACS Appl Mater Interfaces 8:11336–11341
- Zhao J, Xu J, Jian X, Xu J, Gao Z, Song Y-Y (2020) NIR Lightdriven photocatalysis on amphiphilic tio<sub>2</sub> nanotubes for controllable drug release. ACS Appl Mater Interfaces 12:23606–23616
- Santos T, Ferreira R, Quartin E, Boto C, Saraiva C, Bragança J, Peça J, Rodrigues C, Ferreira L, Bernardino L (2017) Blue light potentiates neurogenesis induced by retinoic acid-loaded responsive nanoparticles. Acta Biomater 59:293–302
- Rao S, Chen R, Larocca AA, Christiansen MG, Senko AW, Shi CH, Chiang P-H, Varnavides G, Xue J, Zhou Y, Park S, Ding R, Moon J, Feng G, Anikeeva P (2019) Remotely controlled chemomagnetic modulation of targeted neural circuits. Nat Nanotechnol 14:967–973
- Park J, Jin C, Lee S, Kim JY, Choi H (2019) Magnetically actuated degradable microrobots for actively controlled drug release and hyperthermia therapy. Adv Healthcare Mater 8:1900213
- Ohta S, Kikuchi E, Ishijima A, Azuma T, Sakuma I, Ito T (2020)
   Investigating the optimum size of nanoparticles for their delivery into the brain assisted by focused ultrasound-induced blood-brain barrier opening. Sci Rep 10
- Jo S, Sun I-C, Ahn C-H, Lee S, Kim K (2023) Recent trend of ultrasound-mediated nanoparticle delivery for brain imaging and treatment. ACS Appl Mater Interfaces 15:120–137
- Bansal A, Zhang Y (2014) Photocontrolled nanoparticle delivery systems for biomedical applications. Acc Chem Res 47:3052–3060
- Croissant J, Zink JI (2012) Nanovalve-controlled cargo release activated by plasmonic heating. J Am Chem Soc 134:7628–7631
- Neri G, Corsaro C, Fazio E (2020) Plasmon-enhanced controlled drug release from Ag-PMA capsules. Molecules 25:2267



- Baranes K, Shevach M, Shefi O, Dvir T (2016) Gold nanoparticledecorated scaffolds promote neuronal differentiation and maturation. Nano Lett 16:2916–2920
- Yuan M, Wang Y, Qin Y-X (2018) Promoting neuroregeneration by applying dynamic magnetic fields to a novel nanomedicine: Superparamagnetic iron oxide (SPIO)-gold nanoparticles bounded with nerve growth factor (NGF). Nanomed Nanotechnol Biol Med 14:1337–1347
- Zhang S, Qi Y, Yang H, Gong M, Zhang D, Zou L (2013) Optimization of the composition of bimetallic core/shell Fe<sub>2</sub>O<sub>3</sub>/Au nanoparticles for MRI/CT dual-mode imaging. J Nanopart Res 15
- Xu Z, Hou Y, Sun S (2007) Magnetic Core/Shell Fe<sub>3</sub>O<sub>4</sub>/Au and Fe<sub>3</sub>O<sub>4</sub>/Au/Ag Nanoparticles with Tunable Plasmonic Properties. J Am Chem Soc 129:8698–8699
- Albanese A, Chan WCW (2011) Effect of gold nanoparticle aggregation on cell uptake and toxicity. ACS Nano 5:5478–5489
- Yuan M, Wang Y, Qin Y-X (2017) SPIO-Au core-shell nanoparticles for promoting osteogenic differentiation of MC3T3-E1 cells: Concentration-dependence study. J Biomed Mater Res, Part A 105:3350–3359
- Mahmoudi M, Sant S, Wang B, Laurent S, Sen T (2011) Superparamagnetic iron oxide nanoparticles (SPIONs): Development, surface modification and applications in chemotherapy. Adv Drug Deliv Rev 63:24–46
- Yuan M, Feng X, Yan T-H, Chen J, Ma X, Cunha P, Lan S, Li Y, Zhou H-C, Wang Y (2022) Superparamagnetic iron oxideenclosed hollow gold nanostructure with tunable surface plasmon resonances to promote near-infrared photothermal conversion. Adv Compos Hybrid Mater 5:2387–2398
- Juzenas P, Juzeniene A, Kaalhus O, Iani V, Moan J (2002) Noninvasive fluorescence excitation spectroscopy during application of 5-aminolevulinic acid in vivo. Photochem Photobiol Sci 1:745–748
- Chen J, Yuan M, Madison CA, Eitan S, Wang Y (2022) Bloodbrain barrier crossing using magnetic stimulated nanoparticles. J Control Release 345:557–571
- 28. Hu H, Yuan M, Chen J, Fan T, Nguyen N, Madison CA, Yan T, Zhifeng X, Li Y, Eitan S, Zhou H-C, Pellois JP, Wang Y (2023) Physiologically based pharmacokinetic modeling of gold-coated superparamagnetic iron oxide nanoparticles towards brain-targeted therapeutics. Submitted to J Control Release
- Yuan M, Yan T-H, Li J, Xiao Z, Fang Y, Wang Y, Zhou H-C, Pellois J-P (2021) Superparamagnetic iron oxide–gold nanoparticles conjugated with porous coordination cages: Towards controlled drug release for non-invasive neuroregeneration. Nanomed: Nanotechnol Biol Med 35:102392
- 30. Sudik AC, Millward AR, Ockwig NW, Côté AP, Kim J, Yaghi OM (2005) Design, synthesis, structure, and gas (N<sub>2</sub>, Ar, CO<sub>2</sub>, CH<sub>4</sub>, and H<sub>2</sub>) sorption properties of porous metal-organic tetrahedral and heterocuboidal polyhedra. J Am Chem Soc 127:7110–7118
- Kaphan DM, Levin MD, Bergman RG, Raymond KN, Toste FD (2015) A supramolecular microenvironment strategy for transition metal catalysis. Science 350:1235–1238
- Ishida Y, Suzuki J, Akita I, Yonezawa T (2018) Ultrarapid cationization of gold nanoparticles via a single-step ligand exchange reaction. Langmuir 34:10668–10672
- Fang Y, Lian X, Huang Y, Fu G, Xiao Z, Wang Q, Nan B, Pellois JP, Zhou HC (2018) Investigating subcellular compartment targeting effect of porous coordination cages for enhancing cancer nanotherapy. Small 14:1802709
- 34. Yuan M, Wang Y, Qin Y-X (2019) Engineered nanomedicine for neuroregeneration: light emitting diode-mediated superparamagnetic iron oxide-gold core-shell nanoparticles functionalized by nerve growth factor. Nanomed: Nanotechnol Biol Med 21:102052

- Lim J, Yeap SP, Che HX, Low SC (2013) Characterization of magnetic nanoparticle by dynamic light scattering. Nanoscale Res Lett 8:1–14
- Aqil A, Vasseur S, Duguet E, Passirani C, Benoît J-P, Roch A, Müller R, Jérôme R, Jérôme C (2008) PEO coated magnetic nanoparticles for biomedical application. Eur Polymer J 44:3191–3199
- Lombardo SM, Schneider M, Türeli AE, Günday Türeli N (2020)
   Key for crossing the BBB with nanoparticles: the rational design.
   Beilstein J Nanotechnol 11:866–883
- Maia J, Santos T, Aday S, Agasse F, Cortes L, Malva JO, Bernardino L, Ferreira L (2010) Controlling the neuronal differentiation of stem cells by the intracellular delivery of retinoic acid-loaded nanoparticles. ACS Nano 5:97–106
- Ezpeleta I, Irache JM, Stainmesse S, Chabenat C, Gueguen J, Popineau Y, Orecchioni A-M (1996) Gliadin nanoparticles for the controlled release of all-trans-retinoic acid. Int J Pharm 131:191–200
- Bozuyuk U, Yasa O, Yasa IC, Ceylan H, Kizilel S, Sitti M (2018) Light-triggered drug release from 3D-printed magnetic chitosan microswimmers. ACS Nano 12:9617–9625
- Luo D, Carter KA, Razi A, Geng J, Shao S, Giraldo D, Sunar U, Ortega J, Lovell JF (2016) Doxorubicin encapsulated in stealth liposomes conferred with light-triggered drug release. Biomaterials 75:193–202
- 42. Yuan M, Bancroft EA, Chen J, Srinivasan R, Wang Y (2022) Magnetic fields and magnetically stimulated gold-coated superparamagnetic iron oxide nanoparticles differentially modulate 1-type voltage-gated calcium channel activity in midbrain neurons. ACS Appl Nano Mater
- Chen J, Hu H, Wang Y (2023) Magnetic-driven 3D-printed Biodegradable swimming microrobots. Smart Mater Struct
- 44. Xie P, Shi Z, Feng M, Sun K, Liu Y, Yan K, Liu C, Moussa TAA, Huang M, Meng S (2022) Recent advances in radio-frequency negative dielectric metamaterials by designing heterogeneous composites. Adv Compos Hybrid Mater 5:679–695
- Liu M, Wu H, Wu Y, Xie P, Pashameah RA, Abo-Dief HM, El-Bahy SM, Wei Y, Li G, Li W (2022) The weakly negative permittivity with low-frequency-dispersion behavior in percolative carbon nanotubes/epoxy nanocomposites at radio-frequency range. Adv Compos Hybrid Mater 5:2021–2030
- 46. Hao Y, Leng Z, Yu C, Xie P, Meng S, Zhou L, Li Y, Liang G, Li X, Liu C (2023) Ultra-lightweight hollow bowl-like carbon as microwave absorber owning broad band and low filler loading. Carbon 212:118156
- 47. Zhang Z, Liu M, Ibrahim MM, Wu H, Wu Y, Li Y, Mersal GAM, El Azab IH, El-Bahy SM, Huang M (2022) Flexible polystyrene/ graphene composites with epsilon-near-zero properties. Adv Compos Hybrid Mater 5:1054–1066
- Zhang X-D, Wu D, Shen X, Liu P-X, Yang N, Zhao B, Zhang H, Sun Y-M, Zhang L-A, Fan F-Y (2011) Size-dependent in vivo toxicity of PEG-coated gold nanoparticles. Int J Nanomed 2071–81

**Publisher's Note** Springer Nature remains neutral with regard to jurisdictional claims in published maps and institutional affiliations.

Springer Nature or its licensor (e.g. a society or other partner) holds exclusive rights to this article under a publishing agreement with the author(s) or other rightsholder(s); author self-archiving of the accepted manuscript version of this article is solely governed by the terms of such publishing agreement and applicable law.

